# The Synthesis and Electronic Structure of a Novel $[NiS_4Fe_2(CO)_6]$ Radical Cluster: Implications for the Active Site of the [NiFe] Hydrogenases

**Qiang Wang,[a] J. Elaine Barclay,[b] Alexander J. Blake,[a] E. Stephen Davies,[a] David J. Evans,[b] Andrew C. Marr,[a, d] Eric J. L. McInnes,*[c] Jonathan McMaster,*[a] Claire Wilson,[a] and Martin Schröder*[a]**

**Abstract:** A novel [Ni'$S_4$'$Fe_2(CO)_6$] cluster (**1**: '$S_4$' = $(CH_3C_6H_3S_2)_2(CH_2)_3$) has been synthesised, structurally characterised and has been shown to undergo a chemically reversible reduction process at −1.31 V versus $Fc^+$/Fc to generate the EPR-active monoanion $\mathbf{1}^-$. Multifrequency Q-, X- and S-band EPR spectra of $^{61}$Ni-enriched $\mathbf{1}^-$ show a well-resolved quartet hyperfine splitting in the low-field region due to the interaction with a single $^{61}$Ni ($I = 3/2$) nucleus. Simulations of the EPR spectra require the introduction of a single angle of non-coincidence between $g_1$ and $A_1$, and $g_3$ and $A_3$ to reproduce all of the features in the S- and X-band spectra. This behaviour provides a rare example of the detection and measurement of non-coincidence effects from frozen-solution EPR spectra without the need for single-crystal measurements, and in which the S-band experiment is sensitive to the non-coincidence. An analysis of the EPR spectra of $\mathbf{1}^-$ reveals a 24% Ni contribution to the SOMO in $\mathbf{1}^-$, supporting a delocalisation of the spin-density across the $NiFe_2$ cluster. This observation is supported by IR spectroscopic results which show that the CO stretching frequencies, $\nu$(CO), shift to lower frequency by about 70 $cm^{-1}$ when **1** is reduced to $\mathbf{1}^-$. Density functional calculations provide a framework for the interpretation of the spectroscopic properties of $\mathbf{1}^-$ and suggest that the SOMO is delocalised over the whole cluster, but with little S-centre participation. This electronic structure contrasts with that of the Ni-A, -B, -C and -L forms of [NiFe] hydrogenase in which there is considerable S participation in the SOMO.

**Keywords:** cluster compounds · density functional calculations · electronic structure · EPR spectroscopy · hydrogenase · iron · nickel

## Introduction

Methanogenic, acetogenic, photosynthetic, sulfate-reducing and nitrogen-fixing bacteria consume or produce hydrogen according to the reaction $2H^+ + 2e^- \rightleftharpoons H_2$.[1,2] Members of the hydrogenase family of enzymes mediate this interconversion and insights into the catalytic principles of these enzymes may aid the design of new efficient processes to produce molecular hydrogen as a source of clean energy.[2] The hydrogenases may be classified as [NiFe],[2,3] [Fe]-only,[4] or metal-free[5] according to the metal content of their active sites, and X-ray crystallographic studies of the [NiFe] hydrogenases from *Desulfovibrio gigas*,[6,7] *D. vulgaris*,[8,9] *D. fructosovorans*[10] and *D. sulfuricans*[11] reveal a heterobimetallic cluster of Ni and Fe atoms at the catalytic centres of these enzymes. The active site of the "as-isolated" oxidised form of the [NiFe] hydrogenase from *D. gigas* possesses a Ni centre in a distorted square-pyramidal coordination geometry in which three cysteinyl S donors (Cys65, Cys68 and Cys530) and an exogeneous (hydro)oxo ligand occupy the equatorial sites; a fourth cysteinyl S donor (Cys533) occupies the apical position.[7] This leads to an $NiS_4$ geometry

[a] Dr. Q. Wang, Dr. A. J. Blake, Dr. E. S. Davies, Dr. A. C. Marr, Dr. J. McMaster, Dr. C. Wilson, Prof. Dr. M. Schröder
School of Chemistry, The University of Nottingham
Nottingham, NG7 2RD (UK)
Fax: (+44) 115-9513563
E-mail: M.Schroder@nottingham.ac.uk

[b] J. E. Barclay, Dr. D. J. Evans
Department of Biological Chemistry, John Innes Centre
Norwich Research Park, Norwich, NR4 7UH (UK)

[c] Dr. E. J. L. McInnes
EPSRC EPR Service Centre, Department of Chemistry
The University of Manchester, Oxford Road
Manchester, M13 9PL (UK)

[d] Dr. A. C. Marr
Present address: School of Chemistry
The Queen's University of Belfast, Belfast, BT9 5AG (UK)

Supporting information for this article is available on the WWW under http://www.chemeurj.org/ or from the author. The Supporting Information contains coordinates for DFT calculations and Mössbauer spectra for complex **1a**.



DOI: 10.1002/chem.200305738

that is distinctly nonplanar in which the dihedral angle between the planes defined by (Cys65)S-Ni-S(Cys68) and (Cys530)S-Ni-S(Cys533) planes is 69.8°. The Cys530S, Cys533S and (hydro)oxo donors bridge the Ni and Fe centres at the active site of the enzyme and the coordination sphere of the Fe centre is completed by one CO and two CN ligands.[12] The redox chemistry of the active site of [NiFe] hydrogenase is particularly rich and at least nine spectroscopically distinct states associated with four redox levels of the enzyme have been identified.[13] EPR,[3] XAS,[14] IR[12] and Mössbauer[15] spectroscopic studies, as well as density functional theory (DFT) calculations[16,17] have been used to gain insight into the role of these forms in the catalytic cycle, with consensus descriptions of the electronic structure of the redox states of the enzymes now emerging. In particular, it is generally agreed that the Fe centre remains in the formal $Fe^{II}$ state and the Ni centre shuttles between the formal $Ni^{III}$ and $Ni^{II}$ states during catalysis; the Ni-L and Ni-CO forms of the enzyme are described as formal $Ni^{I}$ centers.[17] However, the role of the distorted nonplanar $S_4$ coordination sphere in tuning the electronic structure of the active site of the [NiFe] hydrogenases remains to be defined. Single-crystal EPR spectroscopic studies[18–20] supported by DFT calculations[17,21,22] reveal a considerable S covalency (ca. 24–39%) in the SOMO for the Ni-A, -B, -C and -L forms of the enzyme, suggesting that redox non-innocence of S-donor sites may be important in controlling the catalytic competency of the active site.

The recognition of a [NiFe] heterobimetallic cluster at the active site of the [NiFe] hydrogenases has prompted the synthesis and characterisation of small molecule analogues[23–25] to gain insight into the structural, spectroscopic and catalytic properties of the active site and to develop the chemical principles that underpin the design of new functional synthetic catalysts. [Ni(NHP*n*$Pr_3$('$S_3$')] ['$S_3$'$^{2-}$ = bis(2-sulfanylphenyl) sulfide(2−)] contains a distorted tetrahedral $NiNS_3$ coordination sphere and can catalyse the heterolytic cleavage of $H_2$.[24] This suggests that the distorted $NiS_4$ coordination sphere at the active site of [NiFe] hydrogenase strongly influences the relative energies of the acceptor and donor orbitals that must interact with the σ and σ* orbitals of $H_2$.[24]

We report herein the synthesis and spectroscopic characterisation of the novel redox active trinuclear [Ni'$S_4$'$Fe_2$-$(CO)_6$] clusters, **1** and **2** ('$S_4$' = $(RC_6H_3S_2)_2(CH_2)_3$ R = Me,H for **1** and **2**, respectively), from the precursors **3** and **4** and show that the $NiS_4$ coordination spheres in **1** and **2** are distinctly nonplanar. We have employed multifrequency Q-, X- and S-band EPR spectroscopy, supported by DFT calculations, to elucidate the electronic structure of $\mathbf{1}^-$ and to probe the participation of the S-donor centres in the redox active orbital of $\mathbf{1}^-$ for comparison with the electronic structures of the Ni-A, -B, -C and -L forms of the [NiFe] hydrogenases. Our results show that a distorted $NiS_4$ coordination sphere is not necessarily associated with substantial Ni–S covalency in the redox active orbital.

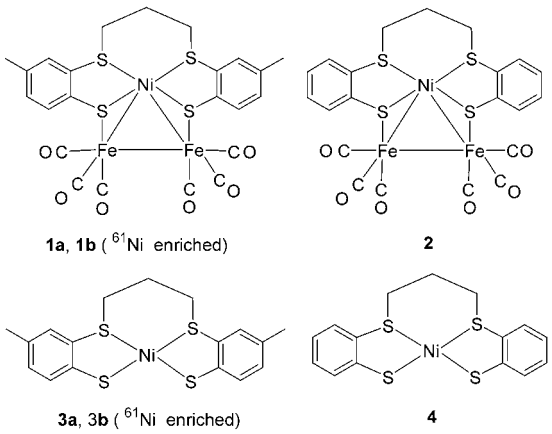


## Results and Discussion

**Preparation of complexes**: Compounds **3a** and **3b** were prepared by a template reaction from (5-methyl-2-mercaptophenyl)thiol and 1,3-dibromopropane with $Ni(OAc)_2 \cdot 4H_2O$ and $Ni(NO_3)_2 \cdot 6H_2O$ (86.2% $^{61}$Ni enriched), respectively.[26,27] The yields of these reactions were improved by the use of excess 1,3-dibromopropane in the synthetic procedure, which could be easily washed from the precipitated product with MeOH. The resolution of the $^1$H NMR spectra for **3a** and **4** is consistent with the formulation of **3a** and **4** as diamagnetic $Ni^{II}S_4$ centres possessing approximate square-planar coordination geometries.[26,27]

After a mixture of **3a** and $[Fe_3(CO)_{12}]$ in $CH_2Cl_2$ was refluxed for 16 h, the IR spectrum of the resulting dark red solution exhibited absorptions at 2035 (s), 2018 (m), 1995 (vs) and 1955 $cm^{-1}$ (s). The removal of $CH_2Cl_2$ from the filtrate and prolonged drying under vacuum yielded a dark red powder. The IR spectrum of this product in $CH_2Cl_2$ exhibited absorptions at 2035 (vs), 1995 (s) and 1955 $cm^{-1}$ (br, s). The reduced intensity of the absorption at 1995 $cm^{-1}$ and the disappearance of the feature at 2018 $cm^{-1}$ after drying the crude product under vacuum suggests that $[Fe(CO)_5]$ is produced as a byproduct of the reaction of **3a** with $[Fe_3(CO)_{12}]$ in $CH_2Cl_2$. This is supported by previous studies that have documented the product distribution for the reactions of $[Fe_3(CO)_{12}]$ with thiols.[28] These reaction mixtures always contain $[Fe(CO)_5]$, probably formed through an interaction of $[Fe(CO)_4]$ fragments with CO produced during the reaction.[28] The reactions of **3b** and **4** with $[Fe_3(CO)_{12}]$ in $CH_2Cl_2$ proceeded in a similar manner to yield **1b** and **2**, respectively, and $[Fe(CO)_5]$ which can be removed under vacuum. The well-resolved $^1$H and $^{13}$C NMR spectra of **1a**, **1b** and **2** and magnetic susceptibility measurements measured by the Evans' method indicate that **1a**, **1b** and **2** are diamagnetic in $CDCl_3$ solution at room temperature.

**The X-ray crystal structures of 1a and 2**: The X-ray crystal structures of **1a** and **2** are shown in Figure 1 and selected bond lengths and angles are presented in Table 1. The Ni centres in **1a** and **2** are coordinated by two *cis*-thiolato and two *cis*-thioether S donors derived from $[(CH_3C_6H_3S_2)_2(CH_2)_3]$ and $[(C_6H_4S_2)_2(CH_2)_3]$, respectively.

  

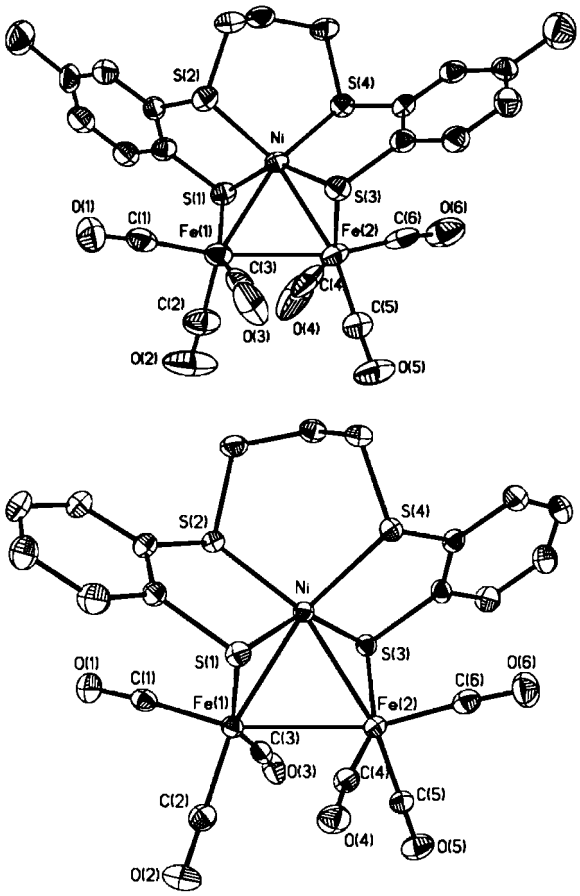


Figure 1. The molecular structure of **1a** (top) and **2** (bottom) with displacement ellipsoids displayed at the 50% probability level. H atoms are omitted for clarity.

Table 1. Selected bond lengths [Å] and angles [°] for **1a**, **2**, and geometry optimised models for **1** and $\mathbf{1}^-$ calculated using DFT.

| | **1a** | **2** | **1** calcd | $\mathbf{1}^-$ calcd |
|---|---|---|---|---|
| Ni–S(1) | 2.1877(13) | 2.1782(9) | 2.256 | 2.245 |
| Ni–S(2) | 2.2495(12) | 2.2599(8) | 2.322 | 2.348 |
| Ni–S(3) | 2.1784(12) | 2.1865(9) | 2.256 | 2.248 |
| Ni–S(4) | 2.2371(13) | 2.2630(9) | 2.329 | 2.342 |
| Fe(1)–S(1) | 2.2580(13) | 2.2623(8) | 2.348 | 2.370 |
| Fe(2)–S(3) | 2.2532(14) | 2.2672(8) | 2.340 | 2.363 |
| Fe(1)···S(3) | 3.3690(14) | 3.3569(12) | 3.646 | 3.721 |
| Fe(2)···S(1) | 3.3408(14) | 3.2705(12) | 3.622 | 3.676 |
| Ni–Fe(1) | 2.4789(9) | 2.4936(8) | 2.546 | 2.670 |
| Ni–Fe(2) | 2.4904(8) | 2.4855(6) | 2.546 | 2.659 |
| Fe(1)–Fe(2) | 2.6435(9) | 2.6279(7) | 2.570 | 2.615 |
| Fe(1)–C(1) | 1.796(5) | 1.806(3) | 1.808 | 1.799 |
| Fe(1)–C(2) | 1.768(6) | 1.790(3) | 1.798 | 1.783 |
| Fe(1)–C(3) | 1.779(5) | 1.770(3) | 1.845 | 1.873 |
| Fe(2)–C(4) | 1.764(6) | 1.786(3) | 1.846 | 1.875 |
| Fe(2)–C(5) | 1.793(5) | 1.789(3) | 1.795 | 1.779 |
| Fe(2)–C(6) | 1.761(6) | 1.817(3) | 1.810 | 1.797 |
| Fe(1)···C(4) | 2.761(6) | 2.720(3) | 2.237 | 2.126 |
| Fe(2)···C(3) | 2.827(5) | 2.780(3) | 2.231 | 2.130 |
| S(1)-Ni-S(2) | 93.07(5) | 92.92(3) | 91.6 | 91.2 |
| S(1)-Ni-S(4) | 106.97(5) | 109.16(3) | 104.1 | 105.4 |
| S(2)-Ni-S(4) | 104.39(5) | 103.77(3) | 103.2 | 102.7 |
| S(1)-Ni-S(3) | 144.88(5) | 143.22(3) | 154.1 | 152.2 |
| S(2)-Ni-S(3) | 109.96(5) | 110.53(3) | 105.5 | 107.4 |
| S(3)-Ni-S(4) | 92.95(5) | 92.81(3) | 91.0 | 90.8 |
| Fe(1)-Ni-Fe(2) | 64.28(3) | 63.71(2) | 59.7 | 60.8 |
| Ni-Fe(2)-Fe(1) | 57.65(2) | 58.30(2) | 59.7 | 60.4 |
| Ni-Fe(1)-Fe(2) | 58.07(2) | 57.993(14) | 59.7 | 60.8 |

These $NiS_4$ units coordinate to an $[Fe_2(CO)_6]$ fragment through two thiolate S-bridging atoms to form trinuclear compounds in which the metal atoms are placed at the corners of an approximate equilateral triangle. The $[Ni'S_4'Fe_2(CO)_6]$ core of these complexes possess approximate $C_2$ symmetry with the twofold axis passing through the Ni centre and the bisector of the Fe–Fe bond. A similar $NiFe_2$ core has been reported in $[Ni(dsdm)\{Fe(CO)_3\}_2]$ ($H_2$dsdm = [*N*,*N*′-dimethyl-*N*,*N*′-bis(2-sulfanylethyl)ethylenediamine]).[25]

The dihedral angles between the S(1)-Ni-S(2) and the S(3)-Ni-S(4) planes (84.04(4) and 85.66(5)° for **1a** and **2**, respectively) indicate a nonplanar coordination environment for the $NiS_4$ units in **1a** and **2**. This is supported by the $NiS_2$ bite angles, which are close to 90° (S(1)-Ni-S(2) = 93.07(5) and 92.93(3)° and S(3)-Ni-S(4) = 92.95(5) and 92.81(3)°, for **1a** and **2**, respectively) and the S(1)-Ni-S(3) and S(2)-Ni-S(4) angles, which are significantly greater than 90° [S(1)-Ni-S(3) = 144.88(5) and 143.22(3)° and S(2)-Ni-S(4) = 104.39(5) and 103.77(3)°, for **1a** and **2**, respectively]. The Ni–S(1) and Ni–S(3) distances (ca. 2.18 Å, Table 1) are typical of formal $Ni^{II}$–S(thiolate) bonds ($|Ni–S| = 2.17$ Å; $\sigma = 0.02$ Å)[29] and the longer Ni–S(2) and Ni–S(4) distances in **1a** and **2** (ca. 2.25 Å, Table 1) lie within the wide range observed for $Ni^{II}$–S(thioether) interactions ($|Ni–S| = 2.36$ Å; $\sigma = 0.11$ Å).[29] The coordination geometry about the Ni centre in **1a** and **2** is similar to that in $[Ni(dsdm)\{Fe(CO)_3\}_2]$ (Ni–S = 2.1602(11) and 2.1724(11) Å and the dihedral angle between the two five-membered rings formed by Ni with the N,C,C,S atoms of each sulfanylethyl portion of dsdm is 87.91(16)°).[25] The coordination geometry of the $NiS_4$ unit in **1a** and **2** contrasts with that of **4**, which possesses approximate square-planar coordination.[27] In **4** the dihedral angle between the S(1)-Ni-S(2) and the S(3)-Ni-S(4) planes (12.2°)[27] is significantly smaller than those in **1a** and **2**, with the $NiS_2$ bite angles close to 90° and the Ni–S(thiolate) and Ni–S(thioether) bond lengths (ca., 2.17 Å) not significantly different from one another. Thus, the geometry of the $NiS_4$ unit in **2** and **1a** distorts away from the approximate square-planar geometry of **3** and **4**[27] in order to accommodate the $Fe_2(CO)_6$ fragment. This distortion, together with the inclusion of two Fe atoms in the coordination sphere of the Ni centre, leads to a coordination geometry about the Ni atom that may be regarded as that of a distorted octahedron.

Each Fe centre in **1a** and **2** is coordinated by one S thiolate donor, one Fe atom and three CO ligands in an approximate square-pyramidal geometry. The Fe–S distances (2.2532(14)–2.2672(8) Å) lie within the range of those for complexes containing $Fe_2(CO)_6$ units coordinated by thiolate ligands ($|Fe–S| = 2.263$ Å; $\sigma = 0.021$ Å);[29] however, in contrast to the majority of these reported structures, the Fe(1)–S(3) and Fe(2)–S(1) distances (3.3690(14) and 3.3408(14) Å, 3.3569(12) and 3.2705(12) Å in **1a** and **2**, respectively) indicate that the thiolate donor atoms do not bridge between the Fe atoms. The mean Fe–C (1.78 Å) and

C–O (1.15 Å) bond lengths in **1a** and **2** are not significantly different from one another and are similar to the corresponding distances for the terminal CO ligands in $[Fe_3(CO)_{12}]$.[30] These data together with the long Fe(1)–C(4) and Fe(2)–C(3) (2.720(3)–2.827(5) Å) and short Fe(1)–C(3) and Fe(2)–C(4) distances (1.764(6)–1.786(3) Å; Table 1) show that the carbonyl ligands defined by atoms C(3) and C(4) in **1a** and **2** bind at the asymmetric extreme in the $Fe_2(CO)_6$ unit in the solid state. The Fe–C and C–O bond lengths in **1a** and **2** are all comparable to those in $[Fe_2(CO)_6(\mu\text{-}SCH_2CH_2CH_2S)]$,[31] whereas, the Fe(1)–Fe(2) bond lengths (2.6435(9) and 2.6279(7) Å in **1a** and **2**, respectively) are significantly longer than that in $[Fe_2(CO)_6(\mu\text{-}SCH_2CH_2CH_2S)]$ (Fe(1)–Fe(1A) = 2.5103(11) Å). This may reflect the absence of a $\mu$-$S_2$ bridging mode in **1a** and **2** and differences in the electronic structure of the Fe centres in these compounds. The Fe(1)–Fe(2) distances in **1a** and **2** (2.6435(9) and 2.6279(7) Å, respectively) are also longer than those in $[Fe_2(CO)_9]$ (2.523(1) Å)[32] and those bridged by CO groups in $[Fe_3(CO)_{12}]$ (2.540(1)–2.554(2) Å),[30] but shorter than those Fe–Fe distances in $[Fe_3(CO)_{12}]$ (2.674(1)–2.684(2) Å)[30] and in [Ni(dsdm){Fe$(CO)_3$}$_2$] (Fe(1)–Fe(2) = 2.6617(8) Å),[25] which lack carbonyl bridging. This last observation suggests that a bonding Fe–Fe interaction is present in **1a** and **2**. The mean Ni–Fe bond length of 2.4871 Å in **1a** and **2** are significantly shorter than the sum of the empirical atomic radii for Ni and Fe (1.35 and 1.40 Å, respectively).[33] Ni–Fe bonding has also been proposed in [Ni(dsdm){Fe$(CO)_3$}$_2$] for which the Ni–Fe(1) and Ni–Fe(2) distances are 2.5130(8) and 2.5061(8) Å, respectively.[25] Thus, it appears that the Ni atom must be included in the coordination spheres of the Fe atoms and that the Ni–Fe interactions should also be considered as metal–metal bonds. Consequently, each Fe centre in **1a** and **2** possesses a six-coordinate, distorted octahedral coordination sphere composed of one Ni and one Fe atom, one thiolato donor and three terminally bound CO ligands.

Table 2. Mössbauer parameters for **1a** and for some representative $[Fe_2(SR)_2(CO)_6]$ (R = alkyl) assemblies.

| Compound | $T$ [K] | $\delta_{Fe}$ [mms$^{-1}$] | $\Delta E_Q$ [mms$^{-1}$] | $\Gamma$ [mms$^{-1}$] | References |
|---|---|---|---|---|---|
| **1a** (solid state) | 298 | −0.02 | 0.66 | 0.13 | this work[a] |
| **1a** (solid state) | 80 | 0.05 | 0.70 | 0.14 | this work[a] |
| **1a** (solution) | 80 | 0.05 | 0.71 | 0.14 | this work[a] |
| [Ni(dsdm){Fe$(CO)_3$}$_2$] | 80 | 0.066 | 0.66 | 0.23 | [25] |
| | | 0.027 | 0.57 | 0.23 | |
| $[Fe_2(SC_3H_6S)(CO)_6]$ | 80 | 0.04 | 0.87 | – | [34] |
| | | 0.03 | 0.70 | – | |
| $[Fe_2\{SCH_2C(CH_2OH)S\}(CO)_6]$ | 80 | 0.01 | 0.95 | – | [34,35] |
| | | 0.01 | 0.75 | – | |
| $[Fe_2(CO)_9]$ | 80 | 0.17 | 0.42 | – | [36] |
| $[Fe_3(CO)_{12}]$ | 80 | 0.115 ($Fe_{1,2}$) | 1.119 | 0.259 | [37] |
| | | 0.057 ($Fe_3$) | 0 | 0.316 | |

[a] Errors $< \pm 0.01$ mms$^{-1}$ for the Mössbauer parameters obtained in this study.

## Spectroscopic and electrochemical investigations of 1 and $1^-$

*Mössbauer spectroscopy*: The Mössbauer spectra of **1a** were recorded as the solid state and as a frozen solution in acetonitrile at 80 K, and the Mössbauer parameters obtained by fitting these spectra with Lorentzian lineshapes are presented in Table 2. The solid-state and solution spectra can be fitted as single quadrupole split doublets with identical isomer shifts ($\delta_{Fe} = 0.05$ mms$^{-1}$) and similar quadrupole splittings ($\Delta E_Q = 0.70$ and 0.71 mms$^{-1}$, respectively) at 80 K. The similarity between solid-state and solution Mössbauer spectra of **1a** indicates that the solid-state structure of **1a** is maintained in acetonitrile at 80 K. The Mössbauer parameters for **1a** fall in the range reported for clusters containing a $[Fe_2(SR)_2(CO)_6]$ (R = alkyl) unit. They show substantial differences to the hyperfine parameters of $[Fe_2(CO)_9]$ and to the equivalent Fe atoms of $[Fe_3(CO)_{12}]$ ($\delta_{Fe} = 0.115$ for $Fe_{1,2}$, Table 2), consistent with an increase in s-electron density at the Fe atoms in **1a**. Thus, the Mössbauer parameters suggest that the distribution of electron density about the $^{57}$Fe nucleus in **1a** is similar to that in other complexes that contain a $\{Fe_2(SR)_2(CO)_6\}$ unit.

*Cyclic voltammetry and coulometry*: The cyclic voltammetry of **1a** shows a chemically reversible reduction process at $E_{1/2} = -1.31$ V versus $Fc^+/Fc$ ($E_p^a - E_p^c = 0.09$ V), a second reduction process at $E_p^c = -1.93$ V versus $Fc^+/Fc$, with an associated oxidation at $E_p^a = -0.68$ V versus $Fc^+/Fc$, and an oxidation process at $E_p^a = 0.24$ V versus $Fc^+/Fc$ with an associated reduction at $E_p^c = -0.75$ V versus $Fc^+/Fc$. A coulometric study at 273 K confirms that the chemically reversible electrochemical couple at $E_{1/2} = -1.31$ V versus $Fc^+/Fc$ (Figure 2) is associated with a one-electron reduction process. This reduction is accompanied by changes in the electronic and vibrational spectra of the test solutions and by the generation of an EPR-active species (see below).

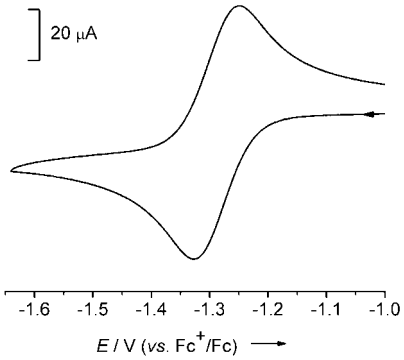


Figure 2. Cyclic voltammogram of **1a** (1 mM) in $CH_2Cl_2$ at 293 K containing $[NnBu_4][BF_4]$ (0.4 M) as supporting electrolyte at a scan rate of 100 mVs$^{-1}$.

The electrochemical reduction of **3a** at 293 K occurs at $E_{1/2} = -1.66$ V versus $Fc^+/Fc$ ($E_p^a - E_p^c = 0.10$ V) and shows marked scan-rate dependence. At slower scan rates

  

($0.02\ V\,s^{-1}$), $I_p^a$ is significantly lowered, whilst at higher scan rates ($0.1–0.3\ V\,s^{-1}$) there is a linear relation of $I_p^a$ with the square root of scan rate. At all scan rates $|I_p^c/I_p^a| > 1.3$ and tends away from unity as the scan rate is decreased. A broad oxidation process at $E_p^a = -0.75$ V versus $Fc^+/Fc$ that is associated with this reduction also develops as the scan rate decreases. The reduction process at $E_{1/2} = -1.66$ V versus $Fc^+/Fc$ is assigned to a formal $Ni^{II/I}$ couple by comparison with the electrochemical data for [Ni{1,3-bis(2-mercaptophenylthio)-2,2-dimethylpropane}], which shows a quasi-reversible $Ni^{II/I}$ reduction process at $E_{1/2} = -0.91$ V versus NHE.[26] The shift of approximately 0.35 V to more positive potential for the first reduction of **1a** relative to that of **3a** demonstrates a significant difference in the nature of their respective LUMOs. This may result from the coordination of the $NiS_4$ unit to the $Fe_2(CO)_6$ fragment and the nonplanarity of the $NiS_4$ unit in **1a**. Furthermore, the reversibility of the reduction process for **1a** suggests that there is no substantial change in molecular geometry between **1a** and $\mathbf{1a}^-$ on the timescale of the electrochemical experiment.

*EPR spectroscopic studies*: Samples of $\mathbf{1a}^-$ and $\mathbf{1b}^-$ for fluid and frozen (120 K) EPR studies were prepared electrochemically and chemically by reduction with cobaltocene from **1a** and **1b**, respectively. The EPR spectra of electrochemically and chemically reduced samples were identical. The X-band spectrum of $\mathbf{1a}^-$ in $CH_2Cl_2$ at room temperature possesses a single feature at $g_{iso} = 2.042$ with a Gaussian linewidth of 17 G, determined by simulation.[38] The spectrum of the 86.2 % $^{61}$Ni-enriched species, $\mathbf{1b}^-$, also exhibits a single feature at $g_{iso} = 2.042$, but with no resolution of the $^{61}$Ni hyperfine interaction observed. However, the peak-to-peak linewidth (ca. 40 G) is much broader for $\mathbf{1b}^-$ than that for $\mathbf{1a}^-$ and must result from an unresolved hyperfine interaction.[39] Therefore, the simulation of the isotropic EPR spectrum of $\mathbf{1b}^-$, with a fixed Gaussian linewidth of 17 G and the magnitude of the isotropic $^{61}$Ni hyperfine coupling as the only variable, allows an accurate determination of $|A_{iso}|$. This analysis gives $|A_{iso}| = 9.5 \times 10^{-4} \pm 0.5 \times 10^{-4}\ cm^{-1}$.

In frozen $CH_2Cl_2$ at 120 K, $\mathbf{1a}^-$ exhibits apparently axial EPR spectra at X- (Figure 3a), S- (Figure 4a) and Q-band (not shown) frequencies. The spectra can be simulated with the $g$ values $g_1 = 2.099$, $g_2 = 2.015$, $g_3 = 2.015$ with Gaussian linewidths as indicated in the figure captions. The equivalent spectra for $\mathbf{1b}^-$ (Figure 3b and 4b) reveal $^{61}$Ni hyperfine coupling in the parallel region due to interaction with the $^{61}$Ni ($I = 3/2$) nucleus.[40] There is no resolution of the $^{61}$Ni hyperfine within the perpendicular region, however, and the linewidths are significantly broadened relative to those of $\mathbf{1a}^-$ due to unresolved hyperfine interactions. Furthermore, there is an additional shoulder on the high-field edge of the perpendicular region of the S-band spectrum of $\mathbf{1b}^-$ (Figure 4b) that is absent in the S-band spectrum of $\mathbf{1a}^-$ (Figure 4a).

We attempted the simultaneous simulation of the Q-, X- and S-band EPR spectra of $\mathbf{1b}^-$ by using $g$ values and linewidths fixed from the spectra of $\mathbf{1a}^-$, and with the (unresolved) perpendicular component of the $^{61}$Ni hyperfine coupling fixed from: $A_{iso} = (A_1 + A_2 + A_3)/3$.

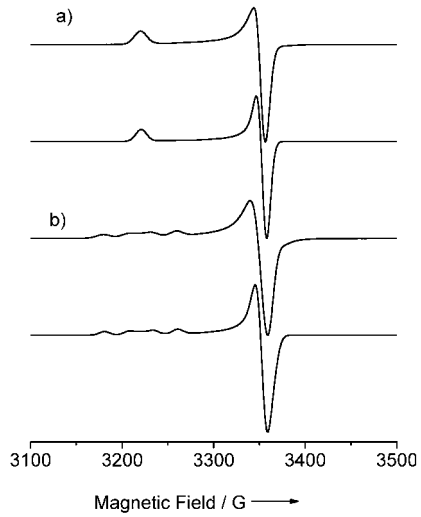


Figure 3. X-band EPR spectra of a) natural abundance $\mathbf{1a}^-$ and b) 86.2 % $^{61}$Ni-enriched $\mathbf{1b}^-$. The top spectra are experimental and the bottom spectra are simulated with the spin-Hamiltonian parameters $g_1 = 2.099$, $g_2 = g_3 = 2.015$, $A_1 = 26.5 \times 10^{-4}\ cm^{-1}$, $A_2 = A_3 = 1.0 \times 10^{-4}\ cm^{-1}$ with an angle of twist about the $g_2/A_2$ axis of 10° and the appropriate weighting of the Ni isotopes. Gaussian linewidths of $W_1 = 12$ G, $W_2 = W_3 = 10$ G.

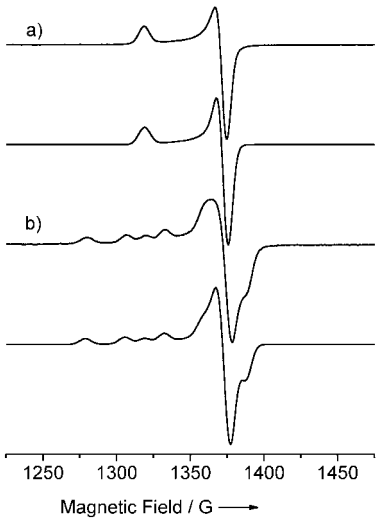


Figure 4. S-band EPR spectra of a) natural abundance $\mathbf{1a}^-$ and b) 86.2 % $^{61}$Ni-enriched $\mathbf{1b}^-$. The top spectra are experimental and the bottom spectra are simulated with the spin-Hamiltonian parameters $g_1 = 2.099$, $g_2 = g_3 = 2.015$, $A_1 = 26.5 \times 10^{-4}\ cm^{-1}$, $A_2 = A_3 = 1.0 \times 10^{-4}\ cm^{-1}$ with an angle of twist about the $g_2/A_2$ axis of 10° and the appropriate weighting of the Ni isotopes. Gaussian linewidths of $W_1 = 8$ G, $W_2 = W_3 = 7$ G.

This analysis gives $|A_1| = 26.5 \times 10^{-4}\ cm^{-1}$, $|A_2| = |A_3| = 1.0 \times 10^{-4}\ cm^{-1}$. Note that this analysis implies that $A_{iso}$, $A_1$, $A_2$ and $A_3$ all have the same sign as one other. These parameters give excellent fits to the X-and Q-band spectra, but do not reproduce the high-field shoulder at S-band. We attempted unsuccessfully to simulate this feature by the introduction of rhombicity in $g_{2,3}$ and/or $A_{2,3}$, including the incorporation of $A_2$ and $A_3$ hyperfine couplings of significant magnitude but of opposite sign, and by attempting to induce an "overshoot" feature at this frequency.[38] We finally con-

sidered the possibility of non-coincidence between two of the principal axes of the **g** and **A** matrices that is allowed in the pseudo-$C_2$ molecular point symmetry of **1b**$^-$ (see below). The introduction of a single angle of non-coincidence between $g_1$ and $A_1$, and between $g_3$ and $A_3$, (i.e., a twist angle of $2\alpha$ about the $g_2/A_2$ axis) mixes the large $A_n$ value with one of the small $A_n$ values (a twist about $g_1/A_1$ would have no effect on the spectra as it would mix numerically identical **A** matrix elements). Inclusion of a twist of $2\alpha = 10°$ about $g_2/A_2$ reproduces *all* of the features in the S-band spectrum (Figure 4b); the position of the shoulder is very sensitive to the value of $2\alpha$ and we estimate an error of $\pm 2°$. The simulated X- and Q-band spectra are insensitive to this angle of non-coincidence.

*UV-visible spectroelectrochemistry*: The reduction of **1a** was monitored spectroelectrochemically by using an optically transparent electrode cell (Figure 5). The observation of isosbestic points at approximately 332, 470, 568 and 639 nm indicates that the reduction of **1a** produces a single species **1a**$^-$ without the involvement of any detectable intermediate. The electrochemical oxidation of **1a**$^-$ returned the UV-visible spectrum to the profile of **1a**, confirming the chemical reversibility of the one-electron electrochemical process on the timescale of the spectroelectrochemical experiment.

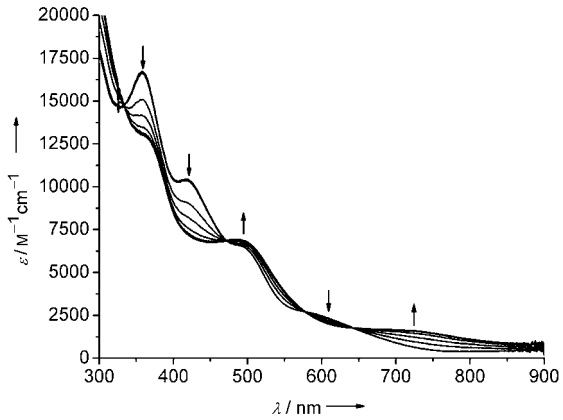


Figure 5. Electronic spectra observed during the one-electron reduction of **1a** at 273 K in $CH_2Cl_2$ containing [N*n*Bu$_4$][$BF_4$] (0.4 M).

Complex **1a** exhibits absorptions at $\lambda_{max}$ ($\varepsilon$) = 359 (16700), 420 (10300) and 490 nm (6600 $M^{-1}cm^{-1}$), and a relatively weak feature in the region at 568 nm (2800 $M^{-1}cm^{-1}$). On reduction to **1a**$^-$ these bands decrease in intensity and new features develop at $\lambda_{max}$ ($\varepsilon$) = 360 (13000), 482 (6900) and 710 nm (1600 $M^{-1}cm^{-1}$). The intensities of the bands in the UV-visible spectra of **1a** and **1a**$^-$ suggest that they result principally from LMCT between orbitals with significant S and metal character. However, we cannot rule out the presence of weaker, underlying bands resulting from transitions within the ligand-field manifold.

*Infra-red spectroscopic studies*: The IR spectra of **1a** and **1a**$^-$, generated by electrochemical reduction of **1a** at 293 K in $CH_2Cl_2$ with [N*n*Bu$_4$][$BF_4$] (0.4 M) as background electrolyte, are shown in Figure 6. The spectra clearly illustrate the differences in $\nu$(CO) associated with the $Fe_2(CO)_6$ fragments of **1a** and **1a**$^-$. The IR spectrum of **1a** can be regenerated by the electrochemical oxidation of **1a**$^-$ or by leaving a solution of **1a**$^-$ within the IR cell to re-oxidise chemically

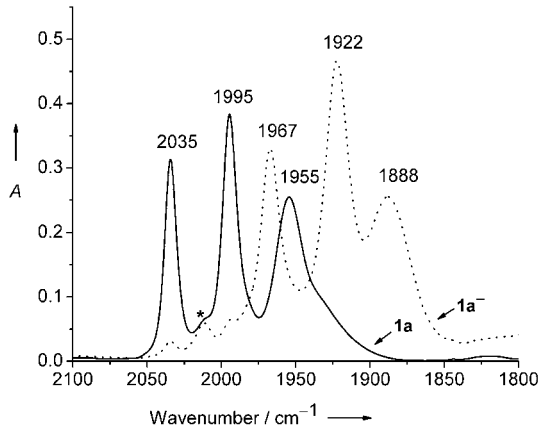


Figure 6. Solution IR spectra recorded for a solution of **1a** in $CH_2Cl_2$ (solid line) and a solution of **1a**$^-$ in $CH_2Cl_2$(dotted line), generated electrochemically from **1a** in $CH_2Cl_2$ (1 mM) containing [N*n*Bu$_4$][$BF_4$] (0.4 M). The band marked with an asterisk in the IR spectra of **1a** and **1a**$^-$ is due to a minor impurity.

over the course of two hours. The mechanism of the chemical re-oxidation is unclear; however, the possible ingression of atmospheric dioxygen into the cell over the period of the experiment cannot be excluded.

Compound **1a** exhibits three strong CO stretching bands (2035, 1995 and 1955 $cm^{-1}$) that are approximately 38 $cm^{-1}$ lower in energy than the CO stretching bands in [$Fe_2(CO)_6$(μ-$SCH_2CH_2CH_2S$)] ($\nu$(CO) = 2072, 2033 and 1993 $cm^{-1}$).[31] The differences in CO stretching frequencies are consistent with a lower formal oxidation state for the Fe centres in **1a** relative to that for the Fe centres in [$Fe_2(CO)_6$(μ-$SCH_2CH_2CH_2S$)], although differences in the $\eta^1$- and $\eta^2$- sulfur donor atom bonding modes for the $Fe_2(CO)_6S_2$ fragments in **1a** and [$Fe_2(CO)_6$(μ-$SCH_2CH_2CH_2S$)] may also contribute to the shift in $\nu$(CO). The CO stretching frequencies in **1a** support terminal CO bonding modes for **1a** in $CH_2Cl_2$ and compare well with $\nu$(CO) in the IR spectrum of **1a** in the solid state (2033, 1990 and 1948 $cm^{-1}$) for which terminal CO bonding modes have been confirmed by X-ray crystallography (see above). The reduction of **1a** to **1a**$^-$ is accompanied by shifts of about 66 to 73 $cm^{-1}$ to lower energy for the CO stretching bands ($\nu$(CO) = 1967, 1922 and 1888 $cm^{-1}$ for **1a**$^-$). These shifts are associated with the increase in electron density across the $Fe_2(CO)_6$ fragment and the congruent increase in Fe π-donation into the π* orbitals of the CO ligands in **1a**$^-$ relative to **1a**. Similar shifts in CO stretching frequencies in the opposite sense have been observed for the one electron oxidation of [$Fe_2${$MeSCH_2C(Me)(CH_2S)_2$}$(CN)_2(CO)_4$]$^{2-}$ to [$Fe_2${$MeSCH_2C(Me)(CH_2S)_2$}$(CN)_2(CO)_4$]$^-$.[34,41] Thus, the reduction of **1a** to **1a**$^-$ results in detectable changes in $\nu$(CO) for the $Fe_2(CO)_6$ fragment and suggests that the re-

  

duction is not centred solely on the $NiS_4$ unit. Furthermore, the similar shifts and band shapes for each of the CO stretching bands for **1a** that accompany the one electron reduction to **1a**$^-$, together with the electrochemical and chemical reversibility of the reduction process, suggests that the integrity of the $Fe_2(CO)_6$ fragment in **1a** is retained in **1a**$^-$.

**Density functional theory geometry optimisations of models of 1 and 1**$^-$: Comparisons between selected bond lengths and angles for the X-ray crystal structures of **1a** and **2** with those of theoretical models of **1** and **1**$^-$ derived from geometry-optimised DFT calculated structures are shown in Table 1. The DFT calculations reproduce the principal features of the experimental geometries of **1a** and **2**, including the nonplanarity of the $NiS_4$ unit (the calculated dihedral angles between the S(1)-Ni-S(2) and S(3)-Ni-S(4) planes = 81.9°). The Ni–S and Fe–S bonds are approximately 0.07 and 0.09 Å longer, respectively, than the corresponding experimental distances in **1a** and **2**, while the calculated Fe–C distances for the terminal CO groups are within 0.01 Å of those found by X-ray crystallography (Table 1). A comparison of the experimental and calculated Fe–C bond lengths for the CO ligands defined by atoms C(3) and C(4) in **1a** and **2** predicts a greater degree of semibridging character for the CO ligands in the calculated structures. The Ni–Fe and Fe–Fe distances are significantly shorter by approximately 0.06 Å in the experimental geometries of **1a** and **2**; a longer metal–metal distance in the gas phase has been observed for unsupported dimers,[42,43] and similar observations have been reported for weak metal–ligand interactions.[43,44] Nevertheless, the similarities between the calculated geometry for **1** in the gas phase and the experimental structures for **1a** and **2** in the condensed phase are sufficient so that the qualitative description of the bonding in **1** is unlikely to be affected adversely by the small differences between the calculated and experimental structures. Furthermore, the reasonable agreement between the calculated and experimental geometries indicates that this DFT method should also be capable of producing a reliable geometry and a reasonable prediction of the electronic structure of a model of **1**$^-$ for which no X-ray crystallographic data are available.

The restricted open-shell geometry optimisation of a model for **1**$^-$ results in a structure that is very similar to the calculated model geometry for **1**. The nonplanarity of the $NiS_4$ unit is maintained; the calculated dihedral angles between the S(1)-Ni-S(2) and S(3)-Ni-S(4) planes are 81.9 and 85.1° for the models of **1** and **1**$^-$, respectively. The calculations predict a shortening of the Ni–S(thiolate) bonds by about 0.01 Å and a lengthening of the Fe–S(thiolate) and Ni–S(thioether) bonds by about 0.02 Å (Table 1) when **1** is reduced to **1**$^-$. Reduction is also accompanied by a significant increase (ca. 0.12 Å) in the Ni–Fe bond lengths and a smaller but significant (ca. 0.08 Å) increase in the Fe–Fe bond distance. The calculated Fe–C distances for the terminal CO groups are slightly shorter in the model of **1**$^-$ relative to the model of **1** ($|Fe–C| = 1.790$ and 1.803 Å for **1**$^-$ and **1**, respectively), while the CO ligands defined by atoms C(3) and C(4) appear to move towards a more symmetrical bridging mode between the two Fe atoms (Table 1).

**The electronic structure of 1 and 1**$^-$: X-ray crystallography has established an approximately equilateral triangular arrangement for the atoms in the $NiFe_2$ core of **1a** and **2**, with the approximate octahedral coordination sphere of each metal centre completed by bridging and/or terminal S-donor and terminal CO ligands (Figure 1). We analysed the electronic structures of **1**$^{0/-1}$ by considering the ligand d-orbital interactions within an $M_3X_{12}$ unit in $D_{3h}$ symmetry in which 12 two-electron σ-donor ligands (X) bind terminally to three metal atoms M to give a psuedo-octahedral coordination sphere for each metal. This situation has been observed experimentally and investigated theoretically for $Os_3(CO)_{12}$ and a qualitative d-orbital splitting diagram for a $M_3X_{12}$ unit, based on these results,[45] is shown in Figure 7. $M_3X_{12}$

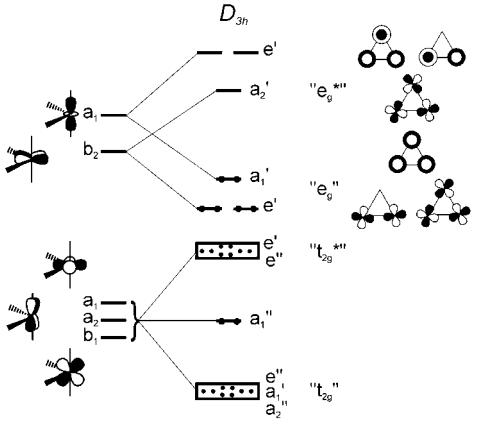


Figure 7. A qualitative d-orbital splitting diagram for a $M_3X_{12}$ unit in $D_{3h}$ symmetry with a 48-EAN electron count.

can be viewed as a combination of three pseudo-octahedral $MX_4$ fragments in which the d-orbitals can be grouped into π pseudo-$t_{2g}$ and σ pseudo-$e_g$ symmetries. The pseudo-$t_{2g}$ orbitals combine to generate one nonbonding, four bonding and four antibonding combinations of $a_1''$ (nonbonding), e″, $a_1'$ and $a_2''$ (bonding) and e′ and e″ (antibonding) symmetries, respectively.

The two σ pseudo-$e_g$ orbitals from each $MX_4$ fragment combine to generate three bonding and three antibonding orbitals of e′ and $a_1'$, and e′ and $a_2'$ symmetries, respectively. For M = Os and X = CO these orbitals are to higher energy than the pseudo-$t_{2g}$ combinations, which are stabilised by M dπ→X back-donation. The effective atomic number (EAN) electron count for the $NiS_4Fe_2(CO)_6$ cores of **1a** and **2** is 48, irrespective of the terminal or bridging nature of the S and CO ligands. Thus, assuming that the d-orbital splitting diagram for the lower symmetry $NiS_4Fe_2(CO)_6$ cores of **1a** and **2** is similar to Figure 7, the pseudo-$t_{2g}$ nonbonding, bonding and antibonding combinations are completely occupied and contribute little to the metal–metal bonding in the $NiFe_2$ unit. This leaves three pairs of electrons that occupy each of the bonding combinations derived from the pseudo-$e_g$ orbitals to generate three formally single M–M bonds within the $NiFe_2$ unit in **1a** and **2**. We have demonstrated that **1a** undergoes an electrochemically quasi-reversible and chemically reversible reduction process at −1.31 V versus $Fc^+$/Fc

(Figure 2) and spectroscopic studies, supported by DFT calculations on models of **1** and $\mathbf{1}^-$, suggest that the structural integrity of **1** is retained in $\mathbf{1}^-$. Thus, the d-orbital splitting diagram (Figure 7) is also relevant for $\mathbf{1}^-$, so that to a first approximation the reduction of **1** to $\mathbf{1}^-$ results in the occupation of a M–M antibonding orbital that may be related in composition to the $a_2'$ ($e_g$*) orbital of $M_3X_{12}$ in $D_{3h}$ symmetry (Figure 7). The precise composition of the SOMO of $\mathbf{1}^-$ will depend strongly on the relative σ-donor and π-donor/acceptor properties of the thiolate, thioether and CO ligands, the relative energies of the Ni and Fe 3d orbitals, and the increase in orbital mixing accompanying the descent in symmetry from $D_{3h}$ to pseudo-$C_2$ symmetry for the $NiS_4Fe_2(CO)_6$ cores of **1a** and **2**. These effects are neglected in this approximate description of the d-orbital splitting in $\mathbf{1}^-$. Nevertheless, this analysis suggests that the SOMO in $\mathbf{1}^-$ lies principally within the plane of the $NiFe_2$ triangle and may be delocalised considerably over the Ni and Fe centres through out-of-phase interactions between the Ni and Fe $3d_{xz}$ orbitals (labelled with reference to the $C_2$ coordinate frame employed in the DFT calculations, see above).

**Interpretation of the EPR parameters**: An interpretation of the EPR parameters obtained from the simultaneous simulation of the S- and X-band EPR spectra of room temperature and frozen solutions of $\mathbf{1a}^-$ and $\mathbf{1b}^-$ permits the assessment of the nature and magnitude of Ni contribution to the SOMO in these compounds. We have demonstrated that, while **1a** has no crystallographically imposed symmetry, it possesses approximate $C_2$ symmetry, with the twofold axis passing through the Ni and the midpoint of the two Fe centres. Furthermore, our spectroscopic, electrochemical and theoretical studies indicate that the structure of **1a** is largely retained in $\mathbf{1a}^-$. $C_2$ symmetry imposes monoclinic EPR symmetry, that is, there is no reason a priori for any of the principal values of the **g** and **A** matrices to be identical.[38] Moreover, one of the $g_n$ and $A_n$ values must be coincident with each other and with the molecular $z$ ($C_2$) axis ($g_{zz}$, $A_{zz}$), but there can be a twist about this axis resulting in non-coincidence between the remaining two $g$ and $A$ values. Hence ($g_{zz}$, $A_{zz}$) must correspond to one of the small $g$ and $A$ matrix elements and $g_1$ and $A_1$ must correspond to an orientation perpendicular to the $C_2$ axis.

In $C_2$ point symmetry, the Ni $3d_{z^2}$, $3d_{x^2-y^2}$ and $3d_{xy}$ orbitals transform as A, whereas the $3d_{xz}$ and $3d_{yz}$ orbitals transform as B. Therefore, in order for the largest hyperfine component (and largest $g$ value) of $\mathbf{1}^-$ to be perpendicular to the $C_2$ axis the Ni contribution to the SOMO must be of B symmetry. Under these conditions the $3d_{xz}$ and $3d_{yz}$ orbitals can mix: $\mathrm{SOMO} = a|xz> + b|yz>$, in which $a$ and $b$ are the linear combination of atomic orbitals (LCAO) coefficients of the Ni $d_{xz}$ and $d_{yz}$ orbitals to the SOMO. It is this mixing that leads to non-coincidence between the axes of the diagonal **g** and **A** matrices. Rieger and co-workers have considered a problem with similar symmetry considerations in the complexes $[Co\{S_2C_2(CF_3)_2\}_2PR_3]$ (R = Ph, OPh) and we follow his analysis.[46] We assume that the Ni contribution to the SOMO is predominantly $3d_{xz}$ with a small admixture of $3d_{yz}$. In the molecular frame ($x$,$y$,$z$), the dipolar part ($A_d$) of the **A** matrix ignoring small spin-orbit coupling corrections is given by Equation (1) in which $P$ is the dipolar coupling parameter for $^{61}$Ni ($= -125.3\times10^{-4}\,\mathrm{cm}^{-1}$).[47] The off-diagonal $xy$ elements result from the d-orbital mixing. This matrix can be diagonalised by rotation by an angle $\alpha$ about the molecular $z$ axis to give Equations (2) and (3).

$$\mathbf{A}^{\mathrm{dip}} = A - A_{\mathrm{iso}} = \frac{2}{7}P\begin{pmatrix} a^2-2b^2 & 3ab & 0 \\ 3ab & b^2-2a^2 & 0 \\ 0 & 0 & a^2+b^2 \end{pmatrix} \quad (1)$$

$$\mathbf{A}^{\mathrm{dip}} = \frac{2}{7}P_d\begin{pmatrix} a^2+b^2 & 0 & 0 \\ 0 & -2b^2-2a^2 & 0 \\ 0 & 0 & a^2+b^2 \end{pmatrix} \quad (2)$$

$$\tan 2\alpha = \frac{-2ab}{a^2-b^2} \quad (3)$$

The matrix elements in Equation (2) correspond to those determined by simulation. Thus, we have $A_1^{\mathrm{dip}} = A_{yy}^{\mathrm{dip}} = A_{yy} - A_{\mathrm{iso}} = \pm 17.0\times10^{-4}\,\mathrm{cm}^{-1}$ and, similarly, $A_{xx}^{\mathrm{dip}} = A_{zz}^{\mathrm{dip}} = \mp 8.5\times10^{-4}\,\mathrm{cm}^{-1}$. Ignoring the spin-orbit coupling corrections we can then estimate the *total* Ni d-orbital contribution to the SOMO from Equation (4):

$$A_{yy}^{\mathrm{dip}} = -{}^4/_7 P(a^2 + b^2) \quad (4)$$

Equation (4) only gives meaningful results [positive values of $(a^2+b^2)$] for positive signs of $A_{\mathrm{iso}}$, $A_1$, $A_2$ and $A_3$. This gives $a^2+b^2 = 0.24$, that is, the SOMO of $\mathbf{1a}^-$ and $\mathbf{1b}^-$ is 24% localised on the Ni ion.

The angle of non-coincidence $2\alpha$ can be related to the ratio of the LCAO coefficients $a$ and $b$ by Equation (5). With $2\alpha = 10°$ we calculate $b^2/a^2 = 0.008$. Thus, the Ni contribution (24%) to the SOMO is overwhelmingly dominated by the $d_{xz}$ orbital and the above analysis is justified.[46]

$$\tan^2\alpha = \frac{b^2}{a^2} \quad (5)$$

**Density functional theory calculations on a model of $\mathbf{1}^-$**: The composition and energy of the SOMO of $\mathbf{1}^-$ derived from spin restricted and unrestricted DFT calculations on a geometry-optimised model of $\mathbf{1}^-$ (see above) are shown in Table 3. Isosurface and contour plots of the SOMO derived from the spin-restricted calculation on a geometry-optimised model of $\mathbf{1}^-$ are shown in Figure 8a and b, respectively. The coordinate frame employed in these calculations is that of the $C_2$ point symmetry described above. The results of both calculations support a delocalised SOMO involving the metal and ligand donor atoms across the $NiS_4Fe_2(CO)_6$ core of $\mathbf{1}^-$. The principal metal contributions are $3d_{xz}$ in character with small admixtures of $3d_{yz}$ for Ni and $3d_{z^2}$ and $3d_{yz}$ for Fe.

There are significant contributions from the thioether and thiolate S donors and there is considerable delocalisation of electron density into the π* orbitals of the CO ligands defined by C(3) and C(4). In the spin-restricted calculation,

  

Table 3. The composition of the SOMO (93a) derived from spin restricted and unrestricted DFT calculations on geometry optimised model structure of $\mathbf{1}^-$. The atom numbering is given in Figures 1 and 8a.

| | Ni(1) | Fe(1) | Fe(2) | S(3) | S(2) | S(4) | S(1) | C(4)O | C(3)O |
|---|---|---|---|---|---|---|---|---|---|
| restricted open shell | | | | | | | | | |
| orbital 93a | 20.3 $d_{xz}$ | 9.8 $d_{xz}$ | 9.7 $d_{xz}$ | 1.7 $p_z$ | 1.7 $p_x$ | 1.6 $p_x$ | 1.4 $p_z$ | | |
| | 3.7 $d_{yz}$ | 5.2 $d_{z^2}$ | 4.5 $d_{z^2}$ | | 1.1 $p_y$ | 1.2 $p_y$ | | | |
| | | 2.1 $d_{yz}$ | 2.2 $d_{yz}$ | | | | | | |
| total % | 24.0 | 17.1 | 16.4 | 1.7 | 2.8 | 2.8 | 1.4 | 4.6 | 3.9 |
| unrestricted open shell | | | | | | | | | |
| orbital 93a | 15.9 $d_{xz}$ | 11.3 $d_{xz}$ | 11.1 $d_{xz}$ | 2.0 $p_z$ | 1.7 $p_x$ | 1.5 $p_x$ | 1.6 $p_z$ | | |
| spin $\alpha$ | 2.4 $d_{yz}$ | 5.6 $d_{z^2}$ | 4.7 $d_{z^2}$ | | 1.1 $p_y$ | 1.1 $p_y$ | | | |
| | | 2.1 $d_{yz}$ | 2.3 $d_{yz}$ | | | | | | |
| total % | 18.3 | 19.0 | 18.1 | 2.0 | 2.8 | 2.6 | 1.6 | 4.9 | 4.9 |

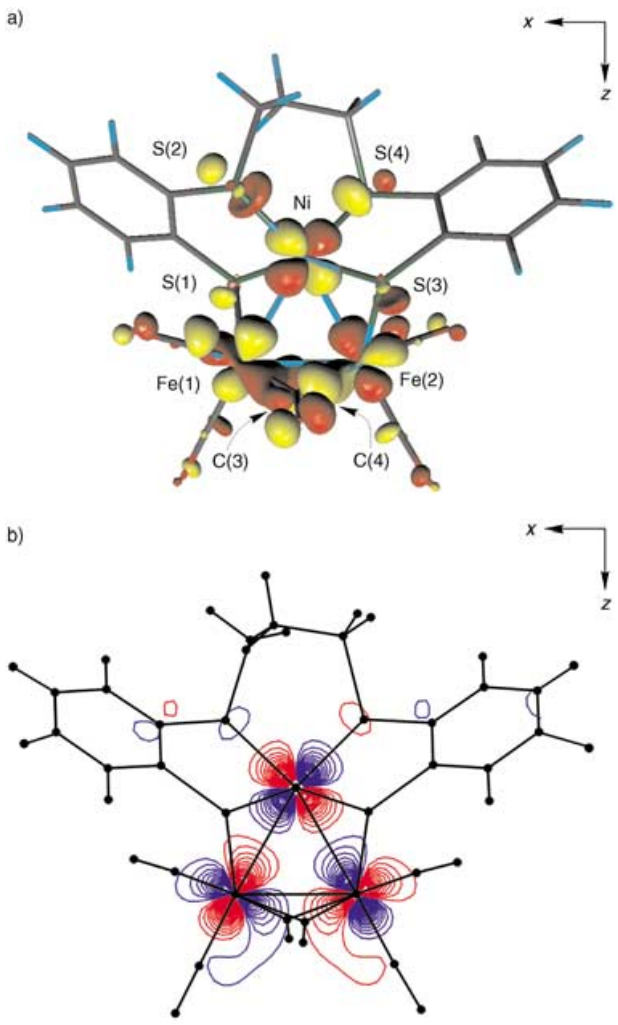


Figure 8. a) Isosurface plot of the SOMO (93a) at the 0.04 e Å$^{-3}$ surface derived from spin-restricted DFT calculations on a geometry optimised model of $\mathbf{1}^-$ and b) a contour plot in the $NiFe_2$ plane for the SOMO (93a).

the total Ni contribution to the SOMO is 24.0%, which is in complete agreement with that derived from the analysis of the EPR parameters for the room temperature and frozen solution S- and X-band spectra for $\mathbf{1}^-$, described above. Furthermore, the DFT calculations also support a dominant Ni $3d_{xz}$ contribution (20.3%) with a smaller Ni $3d_{yz}$ admixture (3.7%). However, the calculated $b^2/a^2$ ratio (0.033) predicts a non-coincidence angle ($2\alpha$) between $g_1$ and $A_1$ of 20.6° that is substantially greater than that observed in the frozen solution S-band EPR spectrum of $\mathbf{1b}^-$ ($2\alpha = 10°$). Similar differences between calculated and experimental non-coincidence angles have been observed for $[Co\{S_2C_2(CF_3)_2\}_2PR_3]$ (R = Ph, OPh) in frozen solution and have been attributed in part to a variety of solvent interactions, which lead to different molecular distortions and thus to different values of $2\alpha$.[46] It is also likely that the solution structure of $\mathbf{1}^-$ differs slightly from that of a model of $\mathbf{1}^-$ geometry optimised in the gas phase and this may also contribute to differences in calculated and experimental values of $2\alpha$. Nevertheless, the agreement between the calculated and experimental Ni contributions to the SOMO in $\mathbf{1}^-$ supports a highly delocalised orbital across the $NiS_4Fe_2(CO)_6$ core of $\mathbf{1}^-$.

The calculated and experimental SOMO in $\mathbf{1}^-$ also supports the qualitative description of the bonding in **1** and $\mathbf{1}^-$ (Figure 7) in which a M–M antibonding orbital, composed of out-of-phase combinations that involve the metal $3d_{xz}$ orbitals, becomes occupied on the reduction of **1** to $\mathbf{1}^-$. This results in the lowering of the formal M–M bond order from 1 in **1** to 0.83 in $\mathbf{1}^-$ and an increase in the Fe–Fe and Ni–Fe bond lengths. This trend is mirrored in the theoretical calculations that show significant increases in the Ni–Fe and Fe–Fe bond lengths (ca. 0.12 Å and 0.08 Å, respectively, Table 1) and decreases in the Ni–Fe and Fe–Fe Mayer bond orders (Table 4) on the reduction of **1** to $\mathbf{1}^-$, calculated for the DFT geometry optimised structures.

Table 4. Mayer bond orders[48] for the geometry optimised model structures of **1** and $\mathbf{1}^-$.

| Model | Ni(1)–Fe(1) | Ni(1)–Fe(2) | Fe(2)–Fe(3) |
|---|---|---|---|
| **1** | 0.5127 | 0.5110 | 0.4281 |
| $\mathbf{1}^-$ (restricted) | 0.3714 | 0.3761 | 0.3766 |

## Conclusion

We have demonstrated that **3a** and **4** react with $[Fe_3(CO)_{12}]$ to form **1a** and **2**, respectively. X-ray crystallographic studies

show that these clusters contain $NiFe_2$ cores in which the $NiS_4$ coordination spheres of **3a** and **4** undergo significant distortions away from planarity to accommodate the $Fe_2(CO)_6$ fragment. The distortion is characterised by an increase in the dihedral angle between the S(1)-Ni-S(2) and S(3)-Ni-S(4) planes (12.2°) in **4** to 84.04(4) and 85.66(5)° in **1a** and **2**, respectively, which indicates a considerable plasticity in the $NiS_4$ coordination sphere. A similarly distorted $NiS_4$ coordination sphere is found at the active sites of the [NiFe] hydrogenases; the dihedral angle between the planes defined by (Cys65)S-Ni-S(Cys68) and (Cys530)S-Ni-S(Cys533) is 69.8° in the unready form of [NiFe] hydrogenase from *D. gigas*[7] and that between the planes defined by (Cys81)S-Ni-S(Cys84) and (Cys546)S-Ni-S(Cys549) is 71.1° in the reduced form of [NiFe] hydrogenase from *D. vulgaris* Miyazaki F.[8] In addition, DFT calculations on potential reaction intermediates in a model of [NiFe] hydrogenase from *D. gigas* suggest that reduction of an unready form of the enzyme to an active form may be accompanied by a change in the Ni coordination sphere which include a decrease in the dihedral angle from 28 to 6° between the planes defined by (Cys65)S-Ni-S(Cys530) and (Cys68)S-Ni-S(Cys533).[49] Thus, the ability of $NiS_4$ coordination spheres to accommodate the geometrical requirements for different redox levels of the active site may be an important prerequisite for the reactivity of the actives sites of the [NiFe] hydrogenases.[50]

Electrochemical studies have demonstrated an electrochemically quasi-reversible one-electron reduction at $E_{1/2} = -1.31$ V versus $Fc^+/Fc$ for **1a** in $CH_2Cl_2$ solution and electronic and IR spectroscopic measurements, supported by DFT calculations, show that this process is chemically reversible. We have employed a multifrequency EPR spectroscopic approach, supported by DFT calculations, to probe the electronic structure of the reduced product $\mathbf{1}^-$. These multifrequency EPR spectroscopic studies provide a rare example[51] of the detection and measurement of non-coincidence effects from frozen solution spectra, without the need for single-crystal measurements. Furthermore for $\mathbf{1a}^-$ and $\mathbf{1b}^-$, the low-microwave-frequency S-band experiment is sensitive to these non-coincidence effects, whereas in other studies[52] the non-coincidence effects were detected in powder spectra at higher Q-band microwave frequencies, while the lower S-, X-band frequencies remained insensitive. Thus, these studies demonstrate that the detection of non-coincidence phenomena is very sensitive to the relative values of the spin-Hamiltonian parameters and the microwave frequency employed in the experiment, and that a multifrequency EPR spectroscopic approach is essential to detect and study these effects.

The EPR parameters, together with the results of the DFT calculations, are consistent with a description of a delocalised SOMO in $\mathbf{1}^-$ with 24.0% Ni and approximately 33% total Fe character with the principle contributions arising from the metal $3d_{xz}$ orbitals. The SOMO lies approximately within the plane of the $NiFe_2$ triangle and is antibonding with respect to the metal–metal interactions. The SOMO also possesses CO–π* antibonding character across the $Fe_2(CO)_6$ fragment (Table 3, Figure 8) making $\nu$(CO) effective reporters of the redox state of the cluster; the one electron reduction of **1a** is accompanied by shifts in $\nu$(CO) of approximately 70 $cm^{-1}$. The relatively low S character (ca. 3–4%) derived from the bridging thiolate S donors in the SOMO of $\mathbf{1}^-$ contrasts with the electronic structures of the Ni-A,[20,22] -B,[20,22] -C[18,21,22] and -L[18,21,22] forms of the [NiFe] hydrogenases derived from single-crystal EPR studies supported by DFT calculations. These studies reveal the majority of the spin density is oriented along the Ni–S(Cys533) bond and only a small amount is at the low-spin formally $Fe^{II}$ centre in the Ni-A, Ni-B and Ni-C forms of the enzyme. The spin density is distributed over the Ni atom (ca. 52%) and the CysS donors with a significant fraction at the Cys533S atom (ca. 24–34%). For the formally $Ni^I$–$Fe^{II}$ Ni-L form, the spin density at the Ni is about 76%, but with negligible distribution onto the Fe centre. The considerable S contributions to the redox active orbitals in the Ni-A, Ni-B, Ni-C and Ni-L forms of the [NiFe] hydrogenases suggest that S redox non-innocence may play an important role in the mode of action of the [NiFe] hydrogenase. Our study has shown that a distorted $NiS_4$ coordination geometry is not necessarily associated with significant S participation in the redox active orbital of Ni centres coordinated by thiolate and thioether ligands. We are currently assessing the reactivity of $\mathbf{1}^-$ towards Brønsted acids to probe whether an $NiFe_2$ cluster that lacks significant S contributions in its redox active orbital can act as a mediator in electrocatalytic $H_2$ evolution.

## Experimental Section

All manipulations, reactions and transfers of samples were conducted under pure argon or $N_2$ atmospheres using standard Schlenk techniques. Dichloromethane was distilled under $N_2$ from $CaH_2$, *n*-hexane from sodium/benzophenone and methanol from magnesium methoxide. Triirondodecacarbonyl, 2-mercaptophenylthiol and 5-methyl-2-mercaptophenylthiol (Aldrich), 1,3-dibromopropane (Acros) and Ni metal, 86.2% enriched in $^{61}$Ni, (Isoflex USA) were used as received. Infrared spectra were recorded on a Nicolet Avatar 360 FTIR spectrometer and solution infra red spectra were recorded using sealed solution cells with either $CaF_2$ or KBr windows. NMR spectra were obtained on a Bruker DPX 300 spectrometer. Elemental analyses were carried out by the Microanalytical Service at the University of Nottingham with an Exeter Analytical Inc CE-440 Elemental analyser and FAB mass spectra were recorded at the EPSRC National Mass Spectrometry Service Centre at University of Wales, Swansea (UK).

Mössbauer spectra were recorded on an ES-Technology MS105 spectrometer using a 900 MBq $^{57}$Co source in a Rh matrix at ambient temperature. Solid samples were ground with boron nitride prior to mounting in the sample holder. Frozen solution samples were prepared by rapidly syringing a solution of the compound in acetonitrile (0.4 $cm^3$) into a Perspex sample cell (18 mm diameter; 2 mm depth) floating on liquid $N_2$. The Mössbauer spectra were referenced to a 25 μm Fe foil at 298 K. Mössbauer parameters were obtained by fitting the experimental data with Lorentzian lineshapes.

Electrochemical measurements were made using an Autolab PGSTAT20 potentiostat. Cyclic voltammograms of 1 mM solutions of each compound in $CH_2Cl_2$ containing $[NnBu_4][BF_4]$ (0.4 M) as the base electrolyte were recorded at 293 K using a glassy carbon working electrode, a Pt wire secondary electrode, and a saturated calomel reference electrode. All potentials were referenced to the $Fc^+/Fc$ couple that was used as an internal standard. When necessary, the $[FeCp^*_2]^+/[FeCp^*_2]$ couple was used as the internal reference to avoid overlapping redox couples. The potentials of these measurements were referenced to the $Fc^+/Fc$ couple by an inde-

  

pendent calibration. Compensation for internal resistance was not applied. All coulometric measurements were performed at 273 K in a $CH_2Cl_2$ containing $[NnBu_4][BF_4]$ (0.4 M); the cell consisted of a Pt/Rh gauze basket working electrode, a Pt/Rh gauze secondary electrode, and a saturated calomel reference electrode.

The UV-visible spectroelectrochemical experiments were carried out at 273 K with an optically transparent electrode mounted in a modified quartz cuvette with an optical pathlength of 0.5 mm. A three-electrode configuration consisting a Pt/Rh gauze working electrode, a Pt wire secondary electrode (in a fritted PTFE sleeve) and a saturated calomel electrode, chemically isolated from the test solution via a bridge tube containing electrolyte solution and terminated in a porous frit, was used in the cell. The potential at the working electrode was controlled by a Sycopel Scientific Ltd. DD10M potentiostat. The UV-visible spectra were recorded on a Perkin Elmer Lambda 16 spectrophotometer. The spectrometer cavity was purged with $N_2$ and temperature control at the sample was achieved by flowing cooled $N_2$ across the surface of the cell.

X-, S- and Q-band EPR spectra were recorded on a Bruker ESP 300E spectrometer. Magnetic fields and microwave frequencies were calibrated with a Bruker ER035M NMR gaussmeter and an EIP microwave counter, respectively. The simulations of the EPR spectra were performed by using in-house software.[38]

Restricted and restricted open-shell geometry optimisations were performed for models of **1** and $\mathbf{1}^-$ using coordinates derived from the X-ray crystal structures of **1a** and **2**, and in which the methyl groups were replaced by H atoms. The coordinate frame used for the calculations places the Ni atom at the origin, the $z$ axis through the bisector of the Fe–Fe bond and the $x$ axis in the plane defined by the Fe-Ni-Fe atoms. No constraints were imposed on the structures during the geometry optimisations. An unrestricted single-point calculation was carried out for a model of $\mathbf{1}^-$ using the coordinates derived from the results of the restricted open-shell geometry optimisation. The calculations were performed using the Amsterdam Density Functional (ADF) suite version 2000.02[53] on an SGI $O_2$ RS12000 computer. The DFT calculations employed Slater type orbital (STO) triple-$\zeta$-plus polarisation basis sets (from the Basis(IV) database of the ADF suite), the frozen core approximation (up to and including 3p for Fe and Ni, 2p for S, and 1s for C and O), and the local density approximation (LDA) with the correlation potential due to Vosko et al.[54] Gradient corrections were performed using the functionals of Becke[55] and Perdew.[56] The program MAYER[48] was used to compute Mayer bond orders for the metal–metal interactions in **1** and $\mathbf{1}^-$ and the program MOLEKEL[57] was used to prepare three-dimensional plots of the electron density.

**Preparation of 1,3-bis[(5-methyl-2-mercaptophenyl)thio]propanatonickel(II) (3a)**: Compound **3a** was prepared by a modification of a method reported previously.[26,27] NaOMe (21 $cm^3$, 0.50 M in MeOH; 10.50 mmol) was added to a solution of (5-methyl-2-mercaptophenyl)thiol (0.81 g, 5.21 mmol) in MeOH (20 $cm^3$). A solution of $Ni(OAc)_2{\cdot}4H_2O$ (0.62 g, 2.60 mmol) in MeOH (15 $cm^3$) was added dropwise and the resultant dark brown solution was stirred for 1 h at room temperature. $Br(CH_2)_3Br$ (0.79 g, 3.90 mmol) was added to the mixture and a brown microcrystalline precipitate formed on stirring over a period of 30 min. The precipitate was collected by filtration, washed with MeOH ($3\times10$ $cm^3$) and dried in vacuo. The product was extracted into $CH_2Cl_2$ and removal of $CH_2Cl_2$ from the filtrate under vacuum afforded the product as a light brown solid (0.69 g, 65%). $^1$H NMR (300 MHz, $CDCl_3$, 298 K): $\delta=2.22$ and 2.70 (m, $2\times1$ H; $SCH_2CH_2CH_2S$), 2.28 (s, 6H; $CH_3$), 3.40 (m, 4H; $SCH_2$), 6.75–7.40 ppm (m, 6H; Ph-$H$); IR (KBr disc): $\tilde{\nu}=3035$ (w), 2914 (m), 2859 (w), 1576 (s), 1545 (w), 1459 (vs), 1419 (m), 1370 (m), 1247 (s), 1216 (w), 1179 (w), 1143 (w), 1108 (s), 1034 (m), 1001 (w), 903 (w), 864 (m), 819 (m), 804 (s), 706 (w), 688 (m), 636 (w), 552 (w), 497 (w), 482 (w), 465 (w), 431 $cm^{-1}$ (m); FAB-MS: $m/z$: 409 [$M^+$]; elemental analysis (%) calcd for $C_{17}H_{18}NiS_4$: C 49.89, H 4.43; found: C 49.71, H 4.22.

**Preparation of $^{61}$Ni-enriched 1,3-bis[(5-methyl-2-mercaptophenyl)thio]-propanatonickel(II) (3b)**: $Ni(NO_3)_2{\cdot}6H_2O$ (86.2% $^{61}$Ni enriched) was prepared as the Ni precursor to **3b**. Ni (86.2% $^{61}$Ni enriched, 0.050 g, 0.82 mmol) was dissolved in $HNO_3$ (20 $cm^3$, 70% w/w). After stirring for 24 h, the green solution was concentrated to about 0.2 $cm^3$, whereupon a green crystalline precipitate formed, which was collected by filtration, washed with ethyl acetate and dried under vacuum. Yield, 0.23 g (95.4%). Compound **3b** was prepared by the same procedure as **3a**, except $Ni(NO_3)_2{\cdot}6H_2O$ (86.2% $^{61}$Ni enriched) was employed instead of $Ni(OAc)_2{\cdot}4H_2O$. $Ni(NO_3)_2{\cdot}6H_2O$ (86.2% $^{61}$Ni enriched, 0.23 g, 0.70 mmol) afforded **3b** in 0.21 g (65.0%) yield. The IR spectrum (KBr disc) of **3b** was essentially identical to that of **3a**.

**Preparation of $[Ni\{(CH_3C_6H_3S_2)_2(CH_2)_3\}(\mu\text{-}S,S')Fe_2(CO)_6]$ (1a) and (1b)**: A solution of **3a** (0.21 g, 0.52 mmol) and $[Fe_3(CO)_{12}]$ (0.23 g, 0.47 mmol) in $CH_2Cl_2$ (18 $cm^3$) was heated to reflux under argon for 16 h. After cooling to room temperature, the dark red solution was filtered to remove a black precipitate. Evaporation of $CH_2Cl_2$ from the filtrate under reduced pressure afforded a dark red powder, which was dried under vacuum. The solid was extracted into MeOH (20 $cm^3$) and the subsequent removal of MeOH under vacuum yielded a dark red powder. Compound **1a** was obtained by recrystallisation from a concentrated $CH_2Cl_2$ solution by solvent diffusion of *n*-hexane. Dark red acicular crystals of **1a** were obtained and were washed with *n*-hexane and dried under vacuum. Yield 0.13 g (40%). $^1$H NMR (300 MHz, $CDCl_3$, 298 K): $\delta=1.80$ (m, 2H; $SCH_2CH_2CH_2S$), 2.35 (s, 3H; $CH_3$), 2.44 (s, 3H; $CH_3$), 2.95 (m, 2H; $SCH_2$), 3.23 (m, 2H; $SCH_2$), 7.05–8.05 ppm (m, 6H; Ph-$H$); $^{13}$C NMR (75 MHz, $CDCl_3$, 298 K): $\delta=212.1$ (s, $CO$), 128.7–157.3 (m, Ph-$C$), 38.6 (s, $SCH_2$), 22.9 (s, $SCH_2CH_2CH_2S$), 20.9 ppm (s, $CH_3$); solution IR ($CH_2Cl_2$): $\tilde{\nu}=2035$ (vs), 1995 (vs), 1955 $cm^{-1}$ (s, br); FAB-MS: $m/z$: 688 [$M^+$], 660 [$M^+-CO$], 632 [$M^+-2CO$], 604 [$M^+-3CO$], 576 [$M^+-4CO$], 548 [$M^+-5CO$], 520 [$M^+-6CO$]; elemental analysis (%) calcd for $C_{23}H_{18}Fe_2NiO_6S_4$: C 40.09, H 2.63; found: C 39.73, H 2.81. Dark red crystals of **1a** suitable for X-ray crystallographic studies were obtained from a saturated MeOH solution of **1a** at −10 °C.

**1b** was prepared from **3b** by the same procedure as for **1a**. The $^1$H, $^{13}$C NMR and IR [$CH_2Cl_2$, $\tilde{\nu}$(CO)] spectra of **1b** are identical to those of **1a**.

**Preparation of $[Ni\{(C_6H_4S_2)_2(CH_2)_3\}(\mu\text{-}S,S')Fe_2(CO)_6]$ (2)**: Compound **4** was prepared using a method reported previously.[27] A solution containing **4** (0.24 g, 0.63 mmol) and $[Fe_3(CO)_{12}]$ (0.29 g, 0.58 mmol) in $CH_2Cl_2$ (20 $cm^3$) was heated to reflux under argon for 16 h. After cooling to room temperature, the dark red solution was filtered to remove a black precipitate. Removal of $CH_2Cl_2$ from the filtrate under reduced pressure afforded a dark red solid, which was dried under vacuum. The solid was purified by column chromatography using a silica gel 60 (Fluka) chromatographic column with $CH_2Cl_2$/petroleum ether (40–60 °C) (6:4 v/v) as eluent. The dark red fraction was collected and the solvent was removed under vacuum to give **2** as a dark red powder (0.13 g, 30%). $^1$H NMR (300 MHz, $CDCl_3$, 298 K): $\delta=1.81$ (m, 2H; $SCH_2CH_2CH_2S$), 2.97 (m, 2H; $SCH_2$) and 3.27 (m, 2H; $SCH_2$), 7.27–8.20 ppm (m, 8H; Ph-$H$); $^{13}$C NMR (75 MHz, $CDCl_3$, 298 K): $\delta=212.0$ (s, $CO$), 127.1–157.3 (m, Ph-$C$), 38.4 (s, $SCH_2$), 22.8 ppm (s, $SCH_2CH_2CH_2S$); solution IR ($CH_2Cl_2$): $\tilde{\nu}=2036$ (vs), 1996 (vs), 1956 $cm^{-1}$ (s, br); FAB MS: $m/z$: 662 [$M^+$+H], 633 [$M^+-CO$], 605 [$M^+-2CO$], 577 [$M^+-3CO$], 549 [$M^+-4CO$], 521 [$M^+-5CO$], 493 [$M^+-6CO$]; elemental analysis (%) calcd for $C_{21}H_{14}Fe_2NiO_6S_4$: C 38.16, H 2.13; found: C 38.34, H 2.09. Dark red crystals suitable for X-ray crystallographic studies were obtained from a saturated MeOH solution of **2** at −10 °C.

**X-ray crystallography**: Crystallographic data for **1a** and **2** are summarised in Table 5. Each crystal was mounted on a dual-stage glass fibre. Diffraction measurements were carried out at 150(2) K on a Bruker SMART 1000 (for **1a**) or a Bruker SMART APEX (for **2**) CCD area detector diffractometer, both equipped with an Oxford Cryosystems open-flow cryostat.[58] Data collection employed graphite-monochromated Mo$K\alpha$ radiation ($\lambda=0.71073$ Å) and $\omega$ scans. Empirical absorption corrections were applied using the program SADABS.[59] Structures were solved by direct methods (**1a**) or heavy-atom Patterson methods (**2**), followed by difference Fourier synthesis, by using SHELXS-97,[60] and refined with SHELXL-97.[61] Hydrogen atoms were placed in calculated positions and constrained to ride on their parent atom with $U_{iso}(H)=xU_{eq}$(parent), in which $x=1.2$ or 1.5.

CCDC-223111 (**1a**) and 223112 (**2**) contain the supplementary crystallographic data for this paper. The crystallographic data can be obtained free of charge via www.ccdc.cam.ac.uk/conts/retrieving.html (or from the Cambridge Crystallographic Data Centre, 12 Union Road, Cambridge CB2 1EZ, UK; fax: (+44)1223-336-033; or e-mail: deposit@ccdc.cam.ac.uk).

Table 5. Selected crystallographic data for **1a** and **2**.

| | **1a** | **2** |
|---|---|---|
| formula | $C_{23}H_{18}Fe_2NiO_6S_4$ | $C_{21}H_{14}Fe_2NiO_6S_4$ |
| $M_r$ | 689.02 | 660.97 |
| crystal system | triclinic | triclinic |
| space group | $P\bar{1}$ | $P\bar{1}$ |
| $a$ [Å] | 8.4534(10) | 10.411(3) |
| $b$ [Å] | 10.7010(13) | 10.869(3) |
| $c$ [Å] | 15.858(2) | 11.894(3) |
| $\alpha$ [°] | 103.521(2) | 97.868(4) |
| $\beta$ [°] | 92.608(2) | 93.629(4) |
| $\gamma$ [°] | 105.271(2) | 111.741(4) |
| $V$ [Å$^3$] | 1336.7(5) | 1228.9(9) |
| $Z$ | 2 | 2 |
| $\rho_{calcd}$ [g cm$^{-3}$] | 1.712 | 1.786 |
| $\mu$ [mm$^{-1}$] | 2.117 | 2.299 |
| crystal size [mm] | $0.18\times0.09\times0.04$ | $0.30\times0.23\times0.10$ |
| $T$ [K] | 150(2) | 150(2) |
| reflections collected | 10465 | 9979 |
| unique reflections ($R_{int}$) | 5841 (0.045) | 5317 (0.032) |
| observed reflections | 3105 | 4692 |
| $R$ [$F>4\sigma(F)$] | 0.044[a] | 0.0340[a] |
| $R_{WF}^2$ (all $F^2$) | 0.083[b] | 0.0805[b] |
| GOF | 0.830 | 1.047 |

[a] $R=\Sigma|(F_o-F_c)|/\Sigma F_o$; [b] $R_{WF}^2=\{\Sigma w(F_o^2-F_c^2)^2/\Sigma[w(F_o^2)^2]\}^{1/2}$.

## Acknowledgement

We thank the BBSRC (UK) for funding. We also thank the University of Nottingham and the CVCP (ORS Awards Scheme) for a studentship to Q. W. We thank EPSRC for provision of the diffractometers and the EPSRC National Mass Spectrometry Service at the University of Wales, Swansea (UK) for mass spectra. We thank Dr. Jing Zhao for help with recording the EPR spectra. The authors dedicate this paper to their friend, mentor and colleague Professor Philip H. Rieger of Brown University who died on April 17th 2004. Phil made seminal contributions in the fields of EPR spectroscopy, electrochemistry and organometallic chemistry, and his approach (reference [46]) was key to the interpretation of the EPR spectra described in this paper.

[1] M. Frey, *Chembiochem* **2002**, *3*, 153–160, and references therein.
[2] *Hydrogen as a Fuel: Learning from Nature* (Eds.: R. Cammack, M. Frey, R. Robson), Taylor & Francis, London, **2001**.
[3] S. P. J. Albracht, *Biochim. Biophys. Acta* **1994**, *1188*, 167–204.
[4] M. W. W. Adams, *Biochim. Biophys. Acta* **1990**, *1020*, 115–145; M. W. W. Adams, E. I. Stiefel, *Curr. Opin. Chem. Biol.* **2000**, *4*, 214–220.
[5] R. K. Thauer, A. Klein, G. C. Hartmann, *Chem. Rev.* **1996**, *96*, 3031–3042.
[6] A. Volbeda, M. H. Charon, C. Piras, E. C. Hatchikian, M. Frey, J. C. Fontecilla-Camps, *Nature* **1995**, *373*, 580–587.
[7] A. Volbeda, E. Garcia, C. Piras, A. L. de Lacey, V. M. Fernandez, E. C. Hatchikian, M. Frey, J. C. Fontecilla-Camps, *J. Am. Chem. Soc.* **1996**, *118*, 12989–12996.
[8] Y. Higuchi, H. Ogata, K. Miki, N. Yasuoka, T. Yagi, *Structure* **1999**, *7*, 549–556.
[9] Y. Higuchi, T. Yagi, N. Yasuoka, *Structure* **1997**, *5*, 1671–1680.
[10] Y. Montet, P. Amara, A. Volbeda, X. Vernede, E. C. Hatchikian, M. J. Field, M. Frey, J. C. Fontecilla-Camps, *Nat. Struct. Biol.* **1997**, *4*, 523–526.
[11] P. M. Matias, C. M. Soares, L. M. Saraiva, R. Coelho, J. Morais, J. Le Gall, M. A. Carrondo, *J. Biol. Inorg. Chem.* **2001**, *6*, 63–81.
[12] A. L. de Lacey, E. C. Hatchikian, A. Volbeda, M. Frey, J. C. Fontecilla-Camps, V. M. Fernandez, *J. Am. Chem. Soc.* **1997**, *119*, 7181–7189; F. Dole, A. Fournel, V. Magro, E. C. Hatchikian, P. Bertrand, B. Guigliarelli, *Biochemistry* **1997**, *36*, 7847–7854; R. P. Happe, W. Roseboom, A. J. Pierik, S. P. J. Albracht, K. A. Bagley, *Nature* **1997**, *385*, 126–126.
[13] M. J. Maroney, P. A. Bryngelson, *J. Biol. Inorg. Chem.* **2001**, *6*, 453–459, and references therein; M. A. Halcrow, G. Christou, *Chem. Rev.* **1994**, *94*, 2421–2481, and references therein.
[14] H. X. Wang, C. Y. Ralston, D. S. Patil, R. M. Jones, W. Gu, M. Verhagen, M. Adams, P. Ge, C. Riordan, C. A. Marganian, P. Mascharak, J. Kovacs, C. G. Miller, T. J. Collins, S. Brooker, P. D. Croucher, K. Wang, E. I. Stiefel, S. P. Cramer, *J. Am. Chem. Soc.* **2000**, *122*, 10544–10552.
[15] K. K. Surerus, M. Chen, J. W. Vanderzwaan, F. M. Rusnak, M. Kolk, E. C. Duin, S. P. J. Albracht, E. Munck, *Biochemistry* **1994**, *33*, 4980–4993.
[16] H. J. Fan, M. B. Hall, *J. Biol. Inorg. Chem.* **2001**, *6*, 467–473, and references therein; P. E. M. Siegbahn, M. R. A. Blomberg, M. W. N. Pavlov, R. H. Crabtree, *J. Biol. Inorg. Chem.* **2001**, *6*, 460–466, and references therein.
[17] M. Stein, W. Lubitz, *Curr. Opin. Chem. Biol.* **2002**, *6*, 243–249.
[18] S. Foerster, M. Stein, M. Brecht, H. Ogata, Y. Higuchi, W. Lubitz, *J. Am. Chem. Soc.* **2003**, *125*, 83–93.
[19] C. Gessner, M. Stein, S. P. J. Albracht, W. Lubitz, *J. Biol. Inorg. Chem.* **1999**, *4*, 379–389; C. Gessner, O. Trofanchuk, K. Kawagoe, Y. Higuchi, N. Yasuoka, W. Lubitz, *Chem. Phys. Lett.* **1996**, *256*, 518–524.
[20] O. Trofanchuk, M. Stein, C. Gessner, F. Lendzian, Y. Higuchi, W. Lubitz, *J. Biol. Inorg. Chem.* **2000**, *5*, 36–44.
[21] M. Stein, W. Lubitz, *Phys. Chem. Chem. Phys.* **2001**, *3*, 5115–5120.
[22] M. Stein, W. Lubitz, *Phys. Chem. Chem. Phys.* **2001**, *3*, 2668–2675; M. Stein, E. V. Lenthe, E. J. Baerends, W. Lubitz, *J. Am. Chem. Soc.* **2001**, *123*, 5839–5840.
[23] M. Y. Darensbourg, E. J. Lyon, J. J. Smee, *Coord. Chem. Rev.* **2000**, *206–207*, 533–561, and references therein; A. C. Marr, D. J. E. Spencer, M. Schröder, *Coord. Chem. Rev.* **2001**, *219*, 1055–1074, and references therein; D. J. Evans, C. J. Pickett, *Chem. Soc. Rev.* **2003**, *32*, 268–275, and references therein; M. C. Smith, J. E. Barclay, S. P. Cramer, S. C. Davies, W. W. Gu, D. L. Hughes, S. Longhurst, D. J. Evans, *J. Chem. Soc. Dalton Trans.* **2002**, 2641–2647; C. J. Curtis, A. Miedaner, R. Ciancanelli, W. W. Ellis, B. C. Noll, M. R. Dubois, D. L. Dubois, *Inorg. Chem.* **2003**, *42*, 216–227; D. Sellmann, F. Geipel, F. Lauderbach, F. W. Heinemann, *Angew. Chem.* **2002**, *114*, 654–656; *Angew. Chem. Int. Ed.* **2002**, *41*, 632–634; N. D. J. Branscombe, A. J. Atkins, A. Marin-Becerra, E. J. L. McInnes, F. E. Mabbs, J. McMaster, M. Schröder, *Chem. Commun.* **2003**, 1098–1099, and references therein; D. Seyferth, R. S. Henderson, M. K. Gallagher, *J. Organomet. Chem.* **1980**, *193*, C75–C78; D. Seyferth, R. S. Henderson, L. C. Song, *Organometallics* **1982**, *1*, 125–133.
[24] D. Sellmann, F. Geipel, M. Moll, *Angew. Chem.* **2000**, *112*, 570–572; *Angew. Chem. Int. Ed.* **2000**, *39*, 561–563.
[25] M. U. Chalbot, A. M. Mills, A. L. Spek, G. J. Long, E. Bouwman, *Eur. J. Inorg. Chem.* **2003**, 453–457.
[26] D. Sellmann, D. Haussinger, F. Knoch, M. Moll, *J. Am. Chem. Soc.* **1996**, *118*, 5368–5374.
[27] D. Sellmann, S. Funfgelder, G. Pohlmann, F. Knoch, M. Moll, *Inorg. Chem.* **1990**, *29*, 4772–4778.
[28] N. S. Nametkin, V. D. Tyurin, M. A. Kukina, *J. Organomet. Chem.* **1978**, *149*, 355–370.
[29] F. H. Allen, *Acta Crystallogr. Sect. B.* **2002**, *58*, 380–388.
[30] L. J. Farrugia, A. L. Gillon, D. Braga, F. Grepioni, *Organometallics* **1999**, *18*, 5022–5033; F. A. Cotton, J. M. Troup, *J. Am. Chem. Soc.* **1974**, *96*, 4155; D. Braga, F. Grepioni, L. J. Farrugia, B. F. G. Johnson, *J. Chem. Soc. Dalton Trans.* **1994**, 2911–2918.
[31] E. J. Lyon, I. P. Georgakaki, J. H. Reibenspies, M. Y. Darensbourg, *Angew. Chem.* **1999**, *111*, 3373–3376; *Angew. Chem. Int. Ed.* **1999**, *38*, 3178–3180.
[32] F. A. Cotton, J. M. Troup, *J. Chem. Soc. Dalton Trans.* **1974**, 800–802.
[33] J. C. Slater, *J. Chem. Phys.* **1964**, *41*, 3199–3204.
[34] M. Razavet, S. C. Davies, D. L. Hughes, J. E. Barclay, D. J. Evans, S. A. Fairhurst, X. M. Liu, C. J. Pickett, *J. Chem. Soc. Dalton Trans.* **2003**, 586–595.
[35] M. Razavet, A. Le Cloirec, S. C. Davies, D. L. Hughes, C. J. Pickett, *J. Chem. Soc. Dalton Trans.* **2001**, 3551–3552.

  

[36] K. Farmery, M. Kilner, R. Greatrex, N. N. Greenwood, *J. Chem. Soc.* **1969**, 2339–2345.
[37] C. G. Benson, G. J. Long, J. W. Kolis, D. F. Shriver, *J. Am. Chem. Soc.* **1985**, *107*, 5297–5298.
[38] F. E. Mabbs, D. Collison, *Electron Paramagnetic Resonance of d-Transition Metal Compounds*, Elsevier, Amsterdam, **1992**.
[39] H. J. Krüger, R. H. Holm, *Inorg. Chem.* **1989**, *28*, 1148–1155.
[40] W. E. Geiger Jr. , C. S. Allen, T. E. Mines, F. C. Senftleber, *Inorg. Chem.* **1977**, *16*, 2003–2008.
[41] M. Razavet, S. C. Davies, D. L. Hughes, C. J. Pickett, *Chem. Commun.* **2001**, 847–848; M. Razavet, S. J. Borg, S. J. George, S. P. Best, S. A. Fairhurst, C. J. Pickett, *Chem. Commun.* **2002**, 700–701.
[42] A. Rosa, A. W. Ehlers, E. J. Baerends, J. G. Snijders, G. T. Velde, *J. Phys. Chem.* **1996**, *100*, 5690–5696.
[43] P. Macchi, L. Garlaschelli, A. Sironi, *J. Am. Chem. Soc.* **2002**, *124*, 14173–14184.
[44] V. Jonas, G. Frenking, M. T. Reetz, *J. Am. Chem. Soc.* **1994**, *116*, 8741–8753.
[45] D. E. Sherwood Jr. , M. B. Hall, *Inorg. Chem.* **1982**, *21*, 3458–3464.
[46] G. B. Carpenter, G. S. Clark, A. L. Rieger, P. H. Rieger, D. A. Sweigart, *J. Chem. Soc. Dalton Trans.* **1994**, 2903–2910.
[47] J. R. Morton, K. F. Preston, *J. Magn. Reson.* **1978**, *30*, 577–582.
[48] A. J. Bridgeman, G. Cavigliasso, L. R. Ireland, J. Rothery, *J. Chem. Soc. Dalton Trans.* **2001**, 2095–2108.
[49] S. Q. Niu, L. M. Thomson, M. B. Hall, *J. Am. Chem. Soc.* **1999**, *121*, 4000–4007.
[50] W. F. Liaw, C. Y. Chiang, G. H. Lee, S. M. Peng, C. H. Lai, M. Y. Darensbourg, *Inorg. Chem.* **2000**, *39*, 480–484.
[51] T. T. Chin, L. I. Sharp, W. E. Geiger, P. H. Rieger, *Organometallics* **1995**, *14*, 1322–1326; C. G. Young, J. H. Enemark, D. Collison, F. E. Mabbs, *Inorg. Chem.* **1987**, *26*, 2925–2927; D. Collison, D. R. Eardley, F. E. Mabbs, K. Rigby, M. A. Bruck, J. H. Enemark, P. A. Wexler, *J. Chem. Soc. Dalton Trans.* **1994**, 1003–1011; B. M. Peake, P. H. Rieger, B. H. Robinson, J. Simpson, *J. Am. Chem. Soc.* **1980**, *102*, 156–163; D. J. Hammack, M. M. Dillard, M. P. Castellani, A. L. Rheingold, A. L. Rieger, P. H. Rieger, *Organometallics* **1996**, *15*, 4791–4797.
[52] D. Collison, D. M. L. Goodgame, M. A. Hitchman, B. Lippert, F. E. Mabbs, E. J. L. McInnes, *Inorg. Chem.* **2002**, *41*, 2826–2833; E. J. L. McInnes, F. E. Mabbs, S. M. Harben, P. D. Smith, D. Collison, C. D. Garner, G. M. Smith, P. C. Riedi, *J. Chem. Soc. Faraday Trans.* **1998**, *94*, 3013–3018.
[53] SC*M*, Vrije Universiteit Amsterdam; http://www.scm.com, Amsterdam, The Netherlands; C. F. Guerra, J. G. Snijders, G. te Velde, E. J. Baerends, *Theor. Chem. Acc.* **1998**, *99*, 391–403; G. te Velde, F. M. Bickelhaupt, S. J. A. van Gisbergen, G. C. Fonseca, E. J. Baerends, J. G. Snijders, T. Ziegler, *J. Comput. Chem.* **2001**, *22*, 931–967.
[54] S. H. Vosko, L. Wilk, M. Nusair, *Can. J. Phys.* **1980**, *58*, 1200–1211.
[55] A. D. Becke, *Phys. Rev. A* **1988**, *38*, 3098–3100.
[56] J. P. Perdew, *Phys. Rev. B* **1986**, *33*, 8822–8824.
[57] S. Portmann, H. P. Luthi, *Chimia* **2000**, *54*, 766–770.
[58] J. Cosier, A. M. Glazer, *J. Appl. Crystallogr.* **1986**, *19*, 105–107.
[59] G. M. Sheldrick, SADABS, Program for Correcting Area Detector Data, Bruker AXS Inc., Madison, Wisconsin, USA, **2001**.
[60] G. M. Sheldrick, SHELXS-97, Program for Crystal Structure Solution, University of Göttingen, Göttingen, Germany, **1997**.
[61] G. M. Sheldrick, SHELXL-97, Program for Crystal Structure Refinement, University of Göttingen, Göttingen, Germany, **1997**.

Received: November 21, 2003
Revised: February 5, 2004
Published online: May 18, 2004